Optical frequency domain imaging with a rapidly swept laser in the 1300nm bio-imaging window

Ratheesh Kumar Meleppat*, Murukeshan Vadakke Matham, Seah Leong Keey
Centre for Optics & Laser Engineering, School of Mechanical & Aerospace Engineering, Nanyang Technological University, 50 Nanyang Avenue, Singapore 639798.

ABSTRACT

Optical frequency domain imaging system (OFDI) in the 1300nm biological imaging window is demonstrated by using a high speed frequency swept laser source. The output of the laser with central wave length of 1320nm is continuously tuned over a bandwidth of 100nm with a repetition rate of 16 KHz. The laser source has an instantaneous coherence length of 6mm and delivers an average power of 12mW. Axial resolution ~ 6μm in the biological tissue and peak sensitivity of 110dB are achieved. The experimentally determined values of the imaging parameters such as the axial resolution, sensitivity and depth range are found to be in good agreement with the theoretically estimated values. The developed system is capable of generating the images of size 512x1024 at a rate of 20 frames per second. High resolution and high contrast images of the finger nail and anterior chamber of a pig's eye acquired using the developed OFDI system are presented, which demonstrate the feasibility of the system for in-vivo biomedical imaging applications.

Keywords: Swept source optical coherence tomography, spectral interferometry, optical frequency domain imaging, spectral windowing, wavelength linearization.

1. INTRODUCTION

The rapid advances and developments in the bio-photonics have witnessed the introduction of innovative and promising optical imaging techniques with broad applications in high resolution imaging[1, 2]. Optical coherence tomography (OCT) is a powerful non- invasive and non-contact biomedical imaging modality that enables depth-resolved and in-vivo visualization of internal microstructures of the biological tissues over millimeters of depth. OCT is often referred as the optical counterpart of the ultrasonography, where the measurement is performed based on the magnitude and time delay of the back reflected acoustic signal from the sample. OCT utilizes infrared light instead of low speed acoustic signal and optical interferometry is used to resolve the time delay between the back reflected light from the adjacent layers [3, 4]. Technically, OCT utilizes the optical gating based on the low coherence interferometry to differentiate signals from closely packed layers thereby providing cross sectional and volumetric images of highly scattering tissues. Because of its unique capability to perform subsurface imaging with high resolution and sensitivity, OCT has gained increased attention among researchers and found wide applicability in the areas of biological research, medical practice and material characterization.

The earlier embodiment of this technique called as the time–domain OCT (TD-OCT) relies on the scanning of reference arm of the interferometer to acquire the depth resolved images of the sample [5]. In this case the temporal gating is achieved using a spectrally broadened, incoherent source. Alternatively, Fourier–domain OCT (FDOCT) was proposed; where the depth information is retrieved form the spectral contents of the interferogram without the translatory motion of the reference arm. There are two embodiments for the Fourier-domain OCT, namely spectral domain OCT (SD-OCT) and swept source OCT (SSOCT), based on the scheme through which the spectral components are resolved and detected. The SD-OCT uses a spectrally broadened source similar to the TD-OCT for illumination and spectral components are spatially resolved and detected by a grating in conjunction with line scan camera [6]. In the case of SS-OCT, which is also known as optical frequency domain imaging (OFDI), a rapidly sweeping narrow bandwidth laser source is used for lighting the system and the spectral fringes are detected by a photodetector in synchronization with the laser sweeping [7]. Recently the research in the OCT regime is more focused on FD-OCT systems because of their capability for imaging with improved speed and sensitivity[8, 9]. Of these FD-OCT schemes, the swept source based OCT (SS-OCT) has been identified as superior than spectral domain OCT (SD-OCT) in performance because of major advantages such as the reduced sensitivity fall-off and lower fringe washout effect caused by the sample motion [10, 11]. Furthermore, the availability of extremely narrow linewidth tunable light sources with higher sweeping rate in

International Conference on Optical and Photonic Engineering (icOPEN 2015), edited by Anand K. Asundi, Yu Fu,
Proc. of SPIE Vol. 9524, 95242R · © 2015 SPIE · CCC code: 0277-786X/15/$18 · doi: 10.1117/12.2190530

association with the balanced detection and sophisticated data acquisition enables high speed and deeper imaging, making it more attractive for many bio-imaging applications.

The wavelength window used for the OCT imaging has a significant impact on the quality and the achievable penetration depth in the biological tissues and it is solely determined based on the wavelength dependent absorption/scattering characteristics of the sample under investigation. Typically ~ 800 nm windows are preferred for the samples such as eye where the water absorption is dominant. Whereas highly scattering tissues such as the skin, improved quality and the depth can be achieved using the 1300nm window [12]. In ocular imaging, 1300nm window is widely used for imaging anterior chamber of the eye, beyond which signal would be attenuated because of the strong absorption.

A high speed and high sensitive imaging demanded by the many bio-imaging applications can be accomplished by the Fourier domain OCT configuration that relies on wavelength swept sources with high repetition rates. In this paper, we describe the systematic illustration of the hardware and software schemes for the development of a swept source based OCT system by discussing its various theoretical and technical aspects. In order to discuss the hardware and software features, an in-house developed SSOCT system has been developed and demonstrated. The developed imaging system is based on a rapidly sweeping wavelength source operating at 16 KHz with a central wavelength of 1320nm and bandwidth 100nm. The dual balanced detection of the spectral fringes with the pair of photodiodes and software based background subtraction allows the imaging system to achieve a better peak signal to noise ratio. An axial resolution of 8.5μm was obtained after the spectral apodization and phase based wavenumber linearization scheme. An excellent peak sensitivity attractive for bio imaging applications was achieved. The developed system has a temporal resolution of 0.05 s that can generate 512X1024 pixel images. The spectral fringes are acquired by the balanced detection scheme followed by the high speed digital sampling. The sampled data is further processed using the digital signal processing techniques including the background subtraction, windowing techniques, calibration and resampling and Fourier transformation in order to construct the cross sectional images.

2. PRINCIPLE

The principle of SS-OCT relies on the low coherence interferometry using tunable wavelength source and the individual spectral components of the low coherence light are sequentially collected by a single element photo detector. The spectral interference signal can be mathematically represented as [13]

$$I(k) = S(k)\left[1 + 2\int_0^\infty a(z)\cos(2knz)dz + \int_0^\infty\int_0^\infty a(z)a(z')\exp[-i2kn(z-z')dzdz']\right] \quad (1)$$

Where S(K) represents spectral intensity distribution of the light source, a(z) is the amplitude of the back scattered signal at depth z and $k=2\pi/\lambda$ is the wave number. According to the Wiener –Khinchine theorem the spectral density function I(k) is the Fourier transform of the auto-correlation function. Hence an inverse Fourier transformation is required to perform in order to retrieve the reflectivity profile of the sample. The depth reflectivity can be expressed as [13]

$$I(z) = FT^{-1}[S(k)] \otimes \{[\delta(z)] + [a(z) + a(-z)] + \frac{1}{4}ACO[a(z) + a(-z)]\} \quad (2)$$

The first term represents the DC term, which is independent of the optical path length and does not carry any structural information and it can be removed by the balanced detection and software based background subtraction. The second term represents the cross correlation term is the desired OCT signal carrying the structural information. The auto-correlation term is generated by the mutual interference of the back reflected signals from different layers within the sample. These terms have negligible effect since they are and generally weaker than OCT signal and weighed by the strong reference signal. Further they are located near to zero path length region and well separated from the center of the OCT signals.

3. IMAGING SETUP- INSTRUMENTATION DETAILS

The schematic of a SSOCT imaging setup is shown in Figure 1. This system consists of a high-speed frequency swept external cavity laser (Thorlabs SL1325-P16), which has a central wavelength of 1320nm and -3dB spectral bandwidth of 100nm. The source has a sweeping rate of 16000 A scans/second and delivers an average optical power of 12mW. The instantaneous linewidth of the laser is found to be 0.290 nm offers a coherence length of 6mm.The output light from the swept source laser is launched into 80/20 coupler (FC) and the 80% of the power is directed towards the Michelson interferometer through a circulator (CIR). Remaining 20% of the light is fed into a built-in Mach-Zehnder interferometer (MZI, ThorlabsINT-MZI-1300) that provides the frequency clock for the calibration purpose. The two arms of the MZI have a path length difference of 3 mm and produces interference fringes which are balanced detected and digitally sampled by one channel of the digitizer as shown in Figure 1. The optical power launched into a fiber-based Michelson interferometer is further divided into the reference and sample arms using a 50/50 coupler (Thorlabs FC1310-70-50-APC). In the reference arm of the interferometer, the light is reflected back into the fiber by a static mirror. The reflectivity is controlled by a neutral density filter (ND) for achieving optimum sensitivity. A variable dispersion compensator (DC) using BK7 glass is introduced at the reference arm to nullify the effect of dispersion induced by the sample [14]. The light in the sample arm is collimated and focused onto the sample surface by a telecentric lens (L) with a long working distance. The back scattered light from the sample is collected through the same imaging lens and finally coupled back to the fiber. The light returning from the end of both paths is recombined at the coupler and generates the interference fringe signal. These fringes are detected by a two balanced photo detectors (BD) (Thorlabs PDB440C).

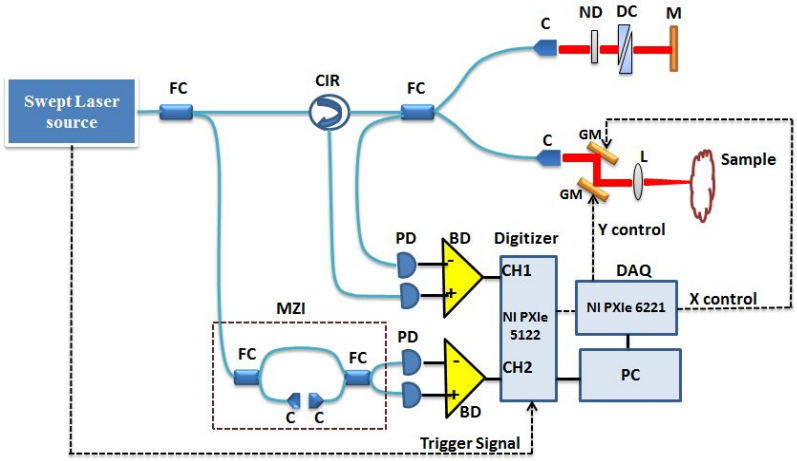

Figure 1. Schematic of the SS-OCT imaging Setup

Both the calibration and OCT signals are acquired through the two channels of a high speed digitizer (PXIe, NI-5122, National Instruments) at a sampling rate of 50MHz with a 14 bit resolution giving rise to 2800 data points. Post data processing such as back ground subtraction, k-space linearization, spectral apodization, inverse Fourier transformation (IFFT), logarithmic compression and gray scale conversion are applied on the signal in order to construct the image. A low speed data acquisition (DAQ) (PXIe, NI-6221, National Instruments) is used to control the galvo mirror based laser beam steering over the sample surface in synchronization with digitizer. The entire signal processing for the synchronization, control and image construction was performed using the LabVIEW software on real time basis.

4. SOFTWARE ARCHITECTURE

Compared to TDOCT, Fourier domain OCT schemes are more computationally intensive as it requires many signal processing stages to construct the image. The major signal processing schemes involves, the background subtraction, spectral apodization, wavelength calibration and resampling of OCT raw signal and inverse FFT followed by the compression and gray scale conversion for the image construction. Figure 2 illustrates process flow of the steps required to create the depth resolved information of a single A-scan from the interferogram.

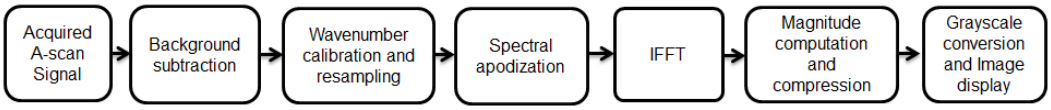

Figure. 2. Process flow of the signal processing steps in SSOCT

The background subtraction involves the recording of the signal by blocking the sample arm prior to every image acquisition and subtracting with the subsequent interference signals. The signal acquired by blocking the sample arm would contain the residual signal from the reference arm and the signal generated by the imperfect symmetry of the balanced detector. Background subtraction helps to reduce DC component and the effect of the residual signal, thereby removing artifacts and increasing the contrast.

The non-linearly sampled OCT data in frequency space on Fourier transformation will lead to the broadening of the point spread function and deterioration of the sensitivity resulting degradation of the image quality. Hence the acquired OCT signal must be resampled into the uniform k-space (frequency) intervals before the Fourier transformation is performed. In order to calibrate the OCT signals at equidistant k-space intervals, fringe signal from an additional Mach-Zehnder interferometer embedded with the laser source was used. The unwrapped phase of this calibration signal is directly proportional to the wavenumber; hence the uniform k-space intervals can be directly derived from the unwrapped phase. The unwrapped of the calibration signal is computed using the Hilbert transform and fitted by a 6th order polynomial relation given by the relation[15].

$$t(k) = a + bk + ck^2 + dk^3 + ek^4 + fk^5 + gk^6 \tag{3}$$

Where the calibration coefficients are found to be as a= 0.0004, b= -0.1494, c=0.0001, d= 7.1284x10^{-7}, e = -6.13x10^{-10}, f= 1.9468x10^{-13} and g=-2.259x10^{-17}. Further, the uniform k-space intervals are computed by the Equation 4 and time index corresponding to the uniform k-intervals are computed using the polynomial relation.

$$k(i) = k(0) + \frac{k(M) - k(0)}{M - 1} i \tag{4}$$

Where i=0,1,2,3…N represents the resampling points. k(0) and k(M) represents the values of wavenumber corresponding to initial and Mth point. The resampling is performed by interpolating OCT signal at the fractional time index values corresponding to the uniformly distributed k-values using the spline interpolation scheme. Figure 3(a), further demonstrates the impact of the calibration scheme on the axial resolution of the OCT signal. In the absence of any calibration scheme the FWHM of the PSF is broadened there by reducing the axial resolution of the system. The calibration scheme based on the spectral phase based scheme narrow down the PSF eventually increases the resolution.

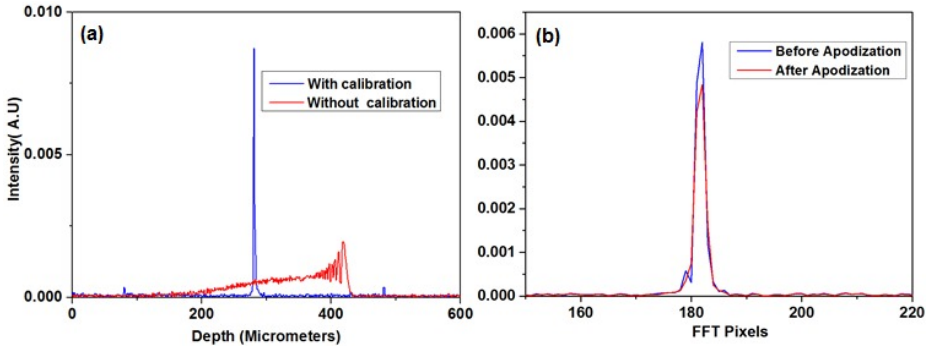

Figure 3. **(a)** Illustration of the effect of calibration on the PSF (b) PSF obtained before and after implementing the spectral apodization scheme.

The non–Gaussian shape of the spectrum profile of the practical OCT sources give rise to the side lobes in the point spread function (PSF) that can blur the adjacent features and induce artifacts in the images [16]. Spectral apodization is typically used to reshape the envelope of the interferogram so as to get the PSF with minimum side lobes and better contrast. Typically, windowing techniques are preferred for reshaping since they are faster and can be performed

digitally. Table 1 shows the comparison of the axial resolution obtained for different windowing functions. From the table it is obvious that, for the developed system, cosine window gives the best performance in terms of the axial resolution and reduction in the peak of PSF. Figure 3(b) shows that side lobes in the PSF are greatly reduced, however, full width at half maximum (FWHM) of the PSF is increased hence the axial resolution is slightly reduced. Further, the peak of the PSF is observed to be reduced after the apodization results in the slight reduction in the SNR

Table 1: Axial resolution obtained for different window functions

Window function	Axial resolution (μm)	Reduction in Peak (-dB)
Cosine	8.7	0.82
Kaiser window	9.8	1.51
Gaussian	9.4	1.40
Super Gaussian	9.2	0.91
Hanning	9.7	1.40
Hamming	9.2	1.30
Blackman	10.4	1.95
Blackman-Harris	10.6	2.45

In Fourier domain OCT, the reflectivity profile of the sample is constructed by performing the inverse fast Fourier transformation of the spectral interferogram sampled linearly in frequency space. Because of the high dynamic range of the OCT signal, pixel intensity range needs to be compressed before displaying it. Generally logarithmic non-linearity is used to perform such compression. The obtained Fourier transformed data is converted from linear scale to dB scale after normalization followed by mapping into the range of [0,255] in order to get the gray scale image.

5. RESULTS AND DISCUSSIONS

5.1 System Performance

5.1.1 Spatial resolutions

Unlike confocal microscopy, the axial and the transverse resolutions in OCT are decoupled. The transverse resolution of the OCT is determined by the size of the beam spot on the sample which depends on the numerical aperture of the focusing optics and the wavelength of the light. A transverse resolution of 25 μm is obtained when a collimated Gaussian beam of diameter of 2.4 mm and a scan lens having 36 mm focal length is used. In OCT, the maximum achievable axial resolution is determined by the center wavelength λ_0 and bandwidth $\Delta\lambda$ of the broadband source used. For a source with Gaussian spectral power density function, the theoretical axial resolution is given by [17]

$$\Delta z = \frac{2\ln 2}{n\pi}\frac{\lambda_0^2}{\Delta\lambda} \tag{5}$$

Practically, the axial resolution is measured as the full width at half maximum (FWHM) value of the PSF obtained. PSF is measured by computing the inverse Fourier transformation (IFFT) of the interference fringes obtained by placing a mirror at the sample arm. For the developed system with λ_0=1320nm and $\Delta\lambda$=100nm, the theoretical axial resolution is found to be ~8 μm in air (n=1). The experimentally obtained resolution by measuring the FWHM of the PSF is found to be 8.7 μm and is very close to the theoretically estimated value. The slight difference in the axial resolution between the theoretically and experimentally determined values is mainly due to the non-Gaussian profile of the source spectrum, in-accuracies associated with the calibration scheme and the slight imbalance of the dispersion in two arms.

5.1.2 Sensitivity

Sensitivity of an OCT system can be defined as the ratio of the incident signal power on the sample to the minimum detectable power that is back reflected from a certain depth corresponding to the path difference Δz. The shot noise limited sensitivity of a SSOCT system is given by [7]

$$\Sigma_{SSOCT} = 10\log\left(\frac{\rho S \Delta t}{2e}\right) \tag{6}$$

Where ρ is the responsivity of the detector, S is the source power, Δt is the sweep time and e is the electronic charge. Using the Equation (8), theoretical sensitivity of ~113dB was estimated for the developed system with a sweep time of 62.5 µs and an incident power of 900 µW on the sample. Experimentally, sensitivity can be quantified as the 20 times the logarithmic ratio of the peak value of the PSF obtained to the standard deviation of the noise floor by blocking the sample arm. Since the direct measurement of the PSF may saturate the detector, hence a combination the mirror and an attenuator is used at the sample arm for the sensitivity measurement. In the developed system, the sensitivity is characterized by placing the mirror and neutral density filter (ND) with optical density (OD) of 3 at the sample arm. Considering the double passage thorough the ND filter, the combination of the mirror and ND filter gives an attenuation of -60dB. The sensitivity can be then calculated as

$$\Sigma_{dB} = 20\log\left(\frac{(i_S(\Delta z))}{\sigma(\Delta z)}\right) + 2.10.OD \tag{7}$$

Where $i_S(\Delta z)$ is the detector current corresponding to the PSF and $\sigma(\Delta z)$ represents the standard deviation of the noise floor. A SNR of 50 dB was measured near to the zero optical path length, leads to a peak sensitivity of 110 dB based on the Equation 7, is agree well with the theoretically computed value. However in SSOCT system, sensitivity decreases with the imaging depth, which is often referred as the sensitivity–roll off is demonstrated in Figure 4. This sensitivity roll-off is an intrinsic effect observed in SSOCT systems, which is caused by the finite instantaneous line width of the wavelength swept laser source.

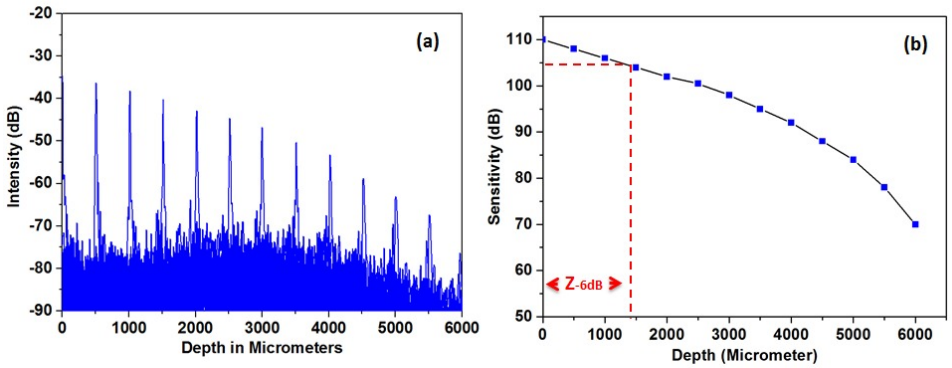

Figure 4. (a) PSF at different depth positions (b) Sensitivity fall-off as function of depth

5.1. 3 Depth range

The maximum imaging depth Z_{max} , that can be achieved by the swept source based OCT system based on the Nyquist criterion is given by [13]

$$z_{max} = \frac{\lambda_0^2}{4n\delta_S\lambda} \tag{8}$$

Where λ_0 is the center wavelength and δ_s represents the spectral sampling interval which is obtained as $\Delta\lambda/N$. Where N is the number of spectral samples in the range $\Delta\lambda$. Accounting to the practical system parameters of the developed system has a theoretical depth of 6mm, which is in agreement with the experimentally observed value from the Figure 4(a). Further, principal imaging range is limited by the instantaneous coherence length of the laser, which is defined as the depth where the sensitivity is dropped by a factor of 1/2 or 6 dB is given by [3]

$$Z_{6dB} = \frac{\ln 2}{\pi} \frac{\lambda_0^2}{\delta_r \lambda} \tag{9}$$

Where the $\delta_r\lambda$ is the spectral resolution of the swept source. Figure 4(b) demonstrates that the practical imaging depth is ~ 1.4mm is close to the theoretically calculated depth of 1.5mm using the Equation 9. The slight difference between theoretically and practically measured value is caused by the phase errors and error associated with the frequency calibration. There are several applications in OCT like imaging of the anterior chamber of the human eye; where optimum roll-off performance is highly desirable to have large effective imaging range. However, in many practical cases the maximum depth range would be limited by the signal losses caused by the absorption and scattering, rather than the sensitivity roll-off.

5.2 Experiment validation

In order to demonstrate the feasibility of the developed OCT system, images of the different biological tissues are presented. The images are acquired at a wavelength swept rate of 16 KHz and an axial resolution of ~8.7 μm in air (n=1), corresponding to the ~ 6.4 μm in tissue samples (n=1.35). It is observed that the dual balanced detection and the background subtraction significantly reduces the DC and autocorrelation thereby offering excellent SNR. Further, the phase based frequency calibration enables highly accurate and stable measurements resulting high quality depth resolved images. Figure 4 shows the images acquired by the developed system with and without implementing the calibration scheme, which demonstrate the strong requirement of a calibration scheme. The image acquired in the absence of calibration scheme is appeared to be blurred as illustrated in Figure 5(a), where no internal features are visible due to the deterioration of the axial resolution and sensitivity. The axial resolution and the sensitivity were greatly improved after implementing the calibration scheme which is evident from the improved quality of the image demonstrated in Figure 5(b).

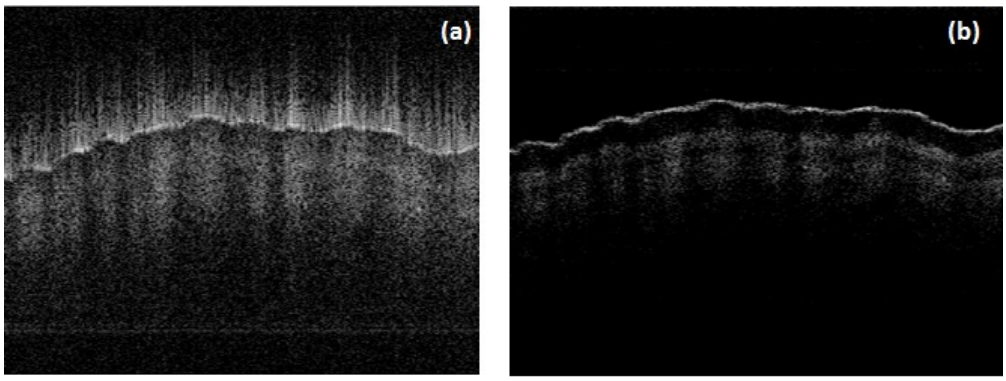

Figure 5. SSOCT image of human palm tissue (a) before calibration (b) after calibration

Figure 6(a) shows the in-vivo image of a human finger nail acquired by the developed SSOCT system demonstrates its capability to generate the high contrast and high resolution images of highly scattering tissues. Various internal features such as the nail plate (NP), nail bed (NB), demis (D), Epidermis(ED) and blood vessels etc. are clearly visible. Figure 6(b) shows the cross sectional image of the iridocorneal angle of a pig's eye. The features such as Iris (IS), Cornea (CA), sclera (SA) and the fine structures within the iridocorneal angle can be observed.

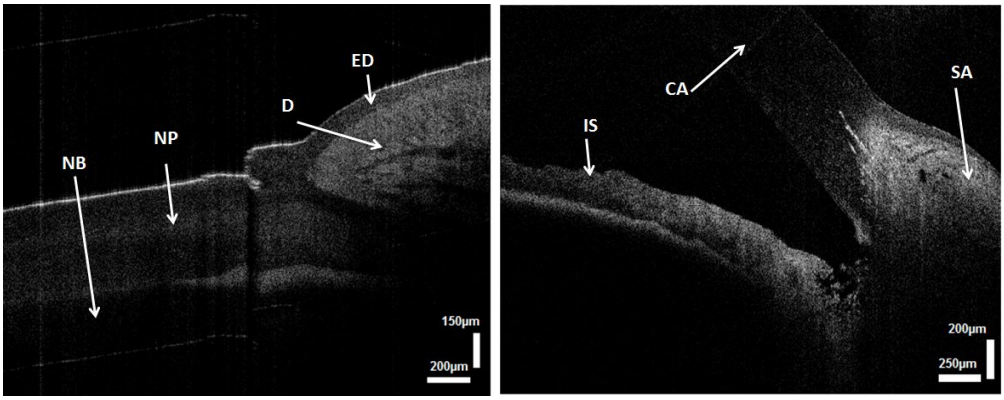

Figure 6. Images acquired by SSOCT system (a) finger nail-skin region (b) iridocorneal angle of a pig's eye.

6. CONCLUSION

In summary, a systematic and comprehensive analysis of the hardware and software configurations for the development of an optical frequency domain imaging system has been demonstrated by discussing necessary theoretical and technical aspects. The low coherence interferometric fringes generated by a fiber optic interferometer are detected by the dual balanced detection scheme followed by digital sampling using a high speed digitizer. An improved SNR has been achieved using the balanced detection and software based background subtraction of A-scan signals. In addition, a spectral phase based wavelength linearization scheme that improves the axial resolution has been demonstrated. An axial resolution of 8.7 μm was obtained after the linearization and spectral apodization. It has been observed that experimentally determined values of the imaging parameters such as axial resolution, sensitivity and imaging depth correlate well with the theoretically computed values. High contrast, high resolution images of the test samples such as human finger nail and iridocorneal angle of the pig's eye demonstrate the feasibility of the developed OFDI system for the various bio-imaging applications.

The authors acknowledge the financial support received through A*STAR-SERC (1121480003) and COLE-EDB funding.

7. REFERENCES

[1] L. K. Seah, U. S. Dinish, S. K. Ong *et al.*, "Time-resolved imaging of latent fingerprints with nanosecond resolution," Optics & Laser Technology, 36(5), 371-376 (2004).

[2] U. S. Dinish, Z. X. Chao, L. K. Seah *et al.*, "Formulation and implementation of a phase-resolved fluorescence technique for latent-fingerprint imaging: theoretical and experimental analysis," Applied Optics, 44(3), 297-304 (2005).

[3] A. F. Fercher, W. Drexler, C. K. Hitzenberger *et al.*, "Optical coherence tomography - principles and applications," Reports on Progress in Physics, 66(2), 239 (2003).

[4] J. G. Fujimoto, C. Pitris, S. A. Boppart *et al.*, "Optical Coherence Tomography: An Emerging Technology for Biomedical Imaging and Optical Biopsy," Neoplasia (New York, N.Y.), 2(1-2), 9-25 (2000).

[5] D. Huang, E. A. Swanson, C. P. Lin *et al.*, "Optical coherence tomography," Science, 254(5035), 1178-81 (1991).

[6] Z. Yaqoob, J. Wu, and C. Yang, "Spectral domain optical coherence tomography: a better OCT imaging strategy," Biotechniques, 39(6 Suppl), S6-13 (2005).

[7] S. Yun, G. Tearney, J. de Boer *et al.*, "High-speed optical frequency-domain imaging," Optics Express, 11(22), 2953-2963 (2003).

[8] R. Leitgeb, C. Hitzenberger, and A. Fercher, "Performance of fourier domain vs. time domain optical coherence tomography," Optics Express, 11(8), 889-894 (2003).

[9] M. Choma, M. Sarunic, C. Yang *et al.*, "Sensitivity advantage of swept source and Fourier domain optical coherence tomography," Optics Express, 11(18), 2183-2189 (2003).

[10] S. H. Yun, G. Tearney, J. de Boer *et al.*, “Motion artifacts in optical coherence tomography with frequency-domain ranging,” Optics Express, 12(13), 2977-2998 (2004).
[11] H. C. Hendargo, R. P. McNabb, A.-H. Dhalla *et al.*, “Doppler velocity detection limitations in spectrometer-based versus swept-source optical coherence tomography,” Biomedical Optics Express, 2(8), 2175-2188 (2011).
[12] J. M. Schmitt, A. Knuttel, M. Yadlowsky *et al.*, “Optical-coherence tomography of a dense tissue: statistics of attenuation and backscattering,” Physics in Medicine and Biology, 39(10), 1705 (1994).
[13] G. Ha¨usler, and M. W. Lindner, ““Coherence Radar” and “Spectral Radar”—New Tools for Dermatological Diagnosis,” Journal of Biomedical Optics, 3(1), 21-31 (1998).
[14] M. Maciejewski, M. Strąkowski, J. Pluciński *et al.*, "Dispersion compensation in optical coherence tomography." 6347, 63471K-63471K-4.
[15] R. K. Meleppat, M. V. Matham, and L. K. Seah, “An efficient phase analysis-based wavenumber linearization scheme for swept source optical coherence tomography systems,” Laser Physics Letters, (2015).
[16] R. Tripathi, N. Nassif, J. S. Nelson *et al.*, “Spectral shaping for non-Gaussian source spectra in optical coherence tomography,” Optics Letters, 27(6), 406-408 (2002).
[17] E. A. Swanson, D. Huang, C. P. Lin *et al.*, “High-speed optical coherence domain reflectometry,” Optics Letters, 17(2), 151-153 (1992).